



H I-rich but low star formation galaxies in MaNGA: physical properties and comparison to control samples

Anubhav Sharma ¹, Karen L. Masters ¹★, David V. Stark,^{1,2} James Garland,¹ Niv Drory,³ Amelia Fraser-McKelvie⁴ and Anne-Marie Weijmans⁵

¹*Department of Physics and Astronomy, Haverford College, 370 Lancaster Avenue, Haverford, PA 19041, USA*

²*Space Telescope Science Institute, 3700 San Martin Drive, Baltimore, MD 21210, USA*

³*McDonald Observatory, The University of Texas at Austin, 1 University Station, Austin, TX 78712, USA*

⁴*European Southern Observatory, Karl-Schwarzschild-Straße 2, 85748 Garching, Germany.*

⁵*School of Physics and Astronomy, University of St Andrews, North Haugh, St Andrews KY16 9SS, UK*

Accepted 2023 September 4. Received 2023 September 4; in original form 2022 July 1

ABSTRACT

Gas-rich galaxies are typically star forming. We make use of H I-MaNGA, a programme of H I follow-up for the Mapping Nearby Galaxies at Apache Point Observatory (MaNGA) survey of the Sloan Digital Sky Surveys, to construct a sample of unusual neutral hydrogen (H I, 21 cm)-rich galaxies that have low star formation rates (SFRs), using infrared colour from the Wide-field Infrared Survey Explorer as a proxy for specific SFR. Out of a set of 1575 MaNGA galaxies with H I-MaNGA detections, we find that 83 (5 per cent) meet our selection criteria to be H I rich with low SFR. We construct two stellar mass-matched control samples: H I-rich galaxies with typical SFR (high SF control) and H I-poor galaxies with low SFR (low H I control). We investigate the properties of each of these samples, comparing physical parameters such as ionization state maps, stellar and ionized gas velocity and dispersion, environment measures, metallicity, and morphology to search for the reasons why these unusual H I-rich galaxies are not forming stars. We find evidence for recent external accretion of gas in some galaxies (via high counter-rotating fractions), along with some evidence for active galactic nucleus (AGN) feedback (from a high central low-ionization emission-line region and/or red geyser fraction), and bar quenching (via an enhanced strong bar fraction). Some galaxies in the sample are consistent with simply having their H I in a high angular momentum, large-radius, low-density disc. We conclude that no single physical process can explain all H I-rich, low-SFR galaxies.

Key words: catalogues – surveys – galaxies: evolution – galaxies: star formation.

1 INTRODUCTION

The question of what quenches star formation (SF) in galaxies is of significant interest to the extragalactic community, as we work to understand the general nature of galaxies. Alongside the accretion of stellar mass via galaxy mergers, galaxies in our Universe grow by the accretion of gas, and by turning that gas into stars. Stars form directly out of molecular hydrogen (H₂), but that molecular hydrogen needs to form out of a neutral atomic hydrogen (H I) reservoir. Since H I is an essential reservoir for SF, it is not surprising that galaxies with rich H I content tend to have higher SF rates (SFRs; e.g. Doyle & Drinkwater 2006; Huang et al. 2012), and it is an interesting question to consider why some galaxies with significant gas reservoirs are not actively forming stars.

While galaxy SFRs are observed to correlate most closely with the molecular hydrogen gas density, e.g. the classic Schmidt–Kennicutt relationship (Kennicutt 1998), and on smaller scales in detailed studies including both resolved H I and CO data (e.g. Schrubba et al. 2011), H I is the dominant mass phase of cold gas in galaxies at the current epoch. For example, studies of the COLD GASS sample

(which includes both molecular and H I gas content; Saintonge et al. 2016) suggest that the position of galaxies in the global SF, stellar-mass plane, the so-called star-forming sequence or SFS, is driven by the availability of a cold (atomic) gas reservoir. For a very recent review of the importance of cold gas content to galaxy evolution, see Saintonge & Catinella (2022). While there is no evidence for a significant population of gas-rich quiescent galaxies (Saintonge & Catinella 2022), there do exist H I-rich galaxies with low SFR. For example, some authors have found that nearly all massive quiescent disc galaxies have typical H I masses [e.g. Zhang et al. (2019), although Cortese et al. (2020) suggest that this may be due to underestimates of extended SF in massive H I discs], and even some quiescent early-type galaxies have H I detections (e.g. Grossi et al. 2009). Understanding why these H I-rich galaxies are not forming stars at typical levels for their H I content may provide important insight into galaxy evolution in general. A previous analysis of 28 H I-rich low-star-forming galaxies by Parkash et al. (2019) revealed that 75 per cent of these galaxies had H α emission consistent with being low-ionization emission-line regions [LIERs, which are linked to old stellar populations or low-luminosity active galactic nuclei (AGNs); e.g. Yan & Blanton 2012]. It was concluded in that work that the presence of H I gas combined with little to no SF might be a precondition for LIER emission (Parkash et al. 2019), but they

* E-mail: klmasters@haverford.edu

left consideration about the main mechanisms of quenching in the sample for future work.

Dynamical effects may also suppress SF in gas-rich systems. Davis et al. (2015) argue that low SF efficiency (SFE) in a sample of gas-rich early-type galaxies may be due to these objects being in a unique phase of evolution where gas is still in the process of streaming towards their centres. Similar effects on SFE due to streaming motions are seen in local regions of M51 (Meidt et al. 2013). Furthermore, increased shock/turbulent heating during a merger may keep H I gas warm, suppressing its ability to contribute to SF (Alatalo et al. 2014; Appleton et al. 2014). The presence of a large bulge may also help stabilize gas discs (Martig et al. 2009; Saintonge et al. 2012).

Previous work on quiescent galaxies with high H I content has suggested that the H I is often distributed in a high angular momentum, large-radius, low-density H I disc (Lemonias et al. 2014; Zhang et al. 2019). At these densities, the time-scales for H I to collapse into H₂ and then H₂ to stars are prohibitively long, and in some galaxies gas may also take a long time to be transported to the inner, denser parts of discs, depending on the details of internal secular evolution and external tidal nudging.

In this paper, we investigate a large sample of H I-rich galaxies with low SFRs in order to attempt to identify the physical reasons why the high H I content is not able to sustain active SF. We investigate the dominant ionizing source of the hydrogen in the galaxies using resolved optical spectroscopy from the Mapping Nearby Galaxies at Apache Point Observatory (MaNGA) survey. We also investigate other measures revealing the physical condition of these unusual galaxies, which we compare with two sets of more typical galaxy control samples (H I-rich and star-forming galaxies and H I-poor and low-star-forming galaxies).

Where physical units are employed, we assume a flat Lambda cold dark matter cosmology with $H_0 = 70 \text{ km s}^{-1} \text{ Mpc}^{-1}$.¹

2 METHODS

2.1 MaNGA data and data products

The sample we use in this work is a subset of galaxies observed by the MaNGA sample (Bundy et al. 2015). MaNGA is a programme under the fourth phase of the Sloan Digital Sky Surveys (SDSS-IV; Blanton et al. 2017), which has mapped the composition and kinematics of a sample of 10 010 nearby galaxies by use of an integral field unit (IFU) on the Sloan Foundation 2.5 m telescope at Apache Point Observatory (for more details on MaNGA instrumentation, telescope, and survey strategy, see Gunn et al. 2006; Smee et al. 2013; Drory et al. 2015; Law et al. 2015, 2016; Yan et al. 2016a, b). MaNGA IFU bundles range from 12 to 32 arcsec in size (with about 30 per cent of the complement being the largest size). The MaNGA sample selection is described in Wake et al. (2017), which explains the primary and secondary samples (designed to have bundle coverage to $1.5r_e$ and $2.5r_e$, respectively, where r_e is the effective radius of the galaxy); we use data from the internal release labelled MaNGA Product Launch 11 (MPL-11), which is identical to the final sample that was made public in the SDSS-IV Data Release 17 (DR17; Abdurro'uf et al. 2022).

¹This is for MaNGA DAP and H I-MaNGA values. Pipe3D quantities are calculated with $H_0 = 71 \text{ km s}^{-1} \text{ Mpc}^{-1}$; however, this introduces at most a 3 per cent systematic, well within our typical statistical error, and we always do relative comparisons between our sample and mass-matched controls.

MaNGA provides fully reduced data IFU data cubes (via the data reduction pipeline; Law et al. 2016), as well as some higher order analysis (maps of velocities, emission lines, etc.) via the data analysis pipeline (or DAP; Westfall et al. 2019); however, further analysis is needed to obtain SFRs, stellar masses, and other parameters of the stellar population. In this work, we make use of the DR17 version v_3_1_1 of the Pipe3D analysis of MaNGA data, which provides such estimates, along with measurements of the ionized gas (e.g. metallicities). The Pipe3D method as applied to MaNGA data is described in Sánchez et al. (2018). Specifically from Pipe3D, we make use of the integrated stellar mass (integrated in the bundle). While a global value of stellar mass might be a better choice to ensure consistency across samples, we find that there is a consistent difference of 0.24 dex between the Pipe3D and a global measure of stellar mass from the NASA Sloan Atlas (NSA; Blanton et al. 2011), a value that is largely explained by differences in initial mass function choice, as explored in detail in Stark et al. (2021). In addition, the distribution of bundle sizes, measured in terms of galaxy effective radius, r_e , is statistically indistinguishable for the three samples introduced in Section 2.4, so we choose to use these stellar masses from MaNGA data directly in our comparison.

From the MaNGA DAP, we make use of the following:

(i) H α ‘rotation speed’, asymmetry, and dispersion from the Gaussian emission-line fit in the DAP. We define the rotation speed measure to be the separation between the HI_CLIP and LO_CLIP (from the DAP, these are the 97.5 and 2.5 per cent percentile values in the MaNGA bundle, respectively, found after clipping 3σ outliers), while the velocity asymmetry is the difference in their absolute values. For velocity dispersion, we use the average value of dispersion measured by the DAP within $1r_e$. This is not corrected for instrumental effects (see Law et al. 2021, for a discussion of the need to do this correction), but we are only using it to compare with control samples, so all should have similar corrections.

(ii) Stellar velocity ‘rotation speed’, asymmetry, and dispersion are taken from the DAP stellar velocity map using similar definitions as for the H α velocity measures above.

Note that we say ‘rotation speed’ as we have not visually checked that these galaxies show symmetric rotation – so this is the equivalent of half the width of a histogram of velocity measures in these maps.

MaNGA targets are selected from the NSA (Blanton et al. 2011), and various NSA values are provided in MaNGA tables. We make use of b/a , the isophotal axial ratio from elliptical Petrosian analysis from the NSA as tabulated in the MaNGA DAP summary table.

Average gas-phase metallicities, $12 + \log \text{O}/\text{H}$, within $1r_e$ are estimated using the N₂O₂ strong-line method of Kewley & Dopita (2002), which uses the [N II] 6585 Å/[O II] 3727 Å flux ratio. Internal extinction corrections are performed on each spaxel using the Balmer decrement, requiring both the H α and H β lines to have flux signal-noise-ratio, $S/N > 3$. $12 + \log(\text{O}/\text{H})$ is calculated in each spaxel, then averaged within $1r_e$. We assume a Balmer decrement of 2.86 (Osterbrock & Ferland 2006) and an extinction curve of O’Donnell (1994). Although there are significant systematic errors in the metallicity zero-point of different strong-line methods, relative comparisons of metallicity, like those performed in this study, should be largely robust against the indicator used (Kewley & Ellison 2008).

2.1.1 Ionization analysis

There are clear trends between the global properties of galaxies and the dominant ionizing source (Sánchez 2020). Generally, the high-energy photons for the ionization of hydrogen come either from the

young stars generated in active SF or from infall of material on to an AGN; however, other ionization mechanisms exist (e.g. the exposed cores of old stars, or shocks). These different mechanisms create different line ratios of common species. The Baldwin, Phillips & Terlevich (1981, hereafter BPT) optical line ratio diagnostic allows astronomers to differentiate whether the ionization comes from SF or AGN, or old stellar populations, or shocks (these last two generally combined together as ‘low-ionization emission-line regions’, or LIERs).

To generate BPT diagrams for the sample, we make use of MARVIN (Cherinka et al. 2019), a PYTHON package designed to work with MaNGA data. Fig. 1 shows two examples of BPT diagrams generated using the MARVIN tool GET_BPT.² MARVIN uses demarcation lines and classification from Kewley et al. (2006) to classify each spaxel with enough line emission (we use the default $S/N > 3$ in all lines in MARVIN, but other choices are possible) as star forming (cyan), LINER (or “low-ionization nuclear emission line region”, treated here as the same as LIER; pink), Seyfert (red), composite (green), or ambiguous (grey). We visually inspected the BPT plots and manually categorized each galaxy using the morphology of the different spaxel classifications. We based our classifications on those described in Belfiore et al. (2016), in summary:

- (i) Star forming: if ‘most’ spaxels are star forming.
- (ii) cLIERs: showing central LIERs surrounded by other spaxel types (see left-hand side of Fig. 1).
- (iii) eLIERs: extended LIERs (see right-hand side of Fig. 1).
- (iv) Seyfert: dominated by Seyfert spaxels.
- (v) Composite+: dominated by composite or ambiguous spaxels (i.e. ‘most’ spaxels ionized by mix of SF and other ionization).
- (vi) Cannot tell: anything else.

2.2 H I-MaNGA

The source of our H I measurements in this work is the H I-MaNGA survey (Masters et al. 2019; Stark et al. 2021), which is making use of the Robert C. Byrd Green Bank Telescope (GBT) to obtain global H I 21 cm line measurements for all MaNGA galaxies $z < 0.05$ to a comparable depth as the ALFALFA (Arecibo Legacy Fast Arecibo L-band Feed Array) survey (Haynes et al. 2018), and using ALFALFA data in the part of the sky where MaNGA and ALFALFA overlap. We use the DR3 sample from H I-MaNGA (Stark et al. 2021), which contains information about H I observations of 6632 unique MaNGA galaxies. These data provide the total H I content and H I line width for MaNGA galaxies; however, as the beams of the radio telescopes at 21 cm are significantly larger than the size of a typical MaNGA galaxy (3 arcmin for Arecibo, and 9 arcmin for GBT compared to < 1 arcmin for most MaNGA galaxies), sometimes H I signals from neighbouring galaxies can be confused. For example, Witherspoon et al. (in preparation) find that some low-mass AGNs that have catalogued H I detections are actually H I poor with nearby H I-rich companions. Stark et al. (2021) provide an estimate of the likelihood of that considering both distance to and redshift and colours of nearby galaxies. A test of this confusion algorithm was provided by Shapiro, Stark & Masters (2022), who conclude that it is a conservative cut – i.e. it removes all potentially confused targets (and some of which are not confused). To be sure that our sample of H I-rich, low-SF galaxies genuinely has its own H I, we therefore use this process to create a clean ‘unconfused’ sample.

2.3 WISE, Galaxy Zoo, and Galaxy environments

We also make use of data from the Wide-field Infrared Survey Explorer (WISE), which mapped the sky at 3.4, 4.6, 12, and 22 μm (W1, W2, W3, and W4) with angular resolutions of 6.1, 6.4, 6.5, and 12.0 arcsec, respectively, in the four bands (Wright et al. 2010). These data can be used to measure SF of our galaxies in a way that is more robust to the effect of dust obscuration than optical or ultraviolet (UV) measures of SF, although there are some disadvantages, such as it missing SF in the outer regions of some galaxies, and also cases where the emission from evolved stars can dominate W3 masking the signal of low levels of SF. However, galaxies with a colour $W2-W3 < 2.0$ have been demonstrated to have a specific SFR ($s\text{SFR} = \text{SFR}/M_* < 10^{-10.4} \text{ yr}^{-1}$ (Parkash et al. 2019)). We make use of magnitudes published in the AllWISE Source Catalog³, choosing the profile-fit photometry galaxies that are small relative to the WISE point spread function (PSF, i.e. point sources), and extended aperture photometry for larger sources. This procedure is recommended by the WISE documentation, which states that profile-fit photometry will underestimate fluxes for extended sources, which include 79 per cent of the MaNGA sample.

We make use of visual morphologies from the Galaxy Zoo (GZ) analysis of SDSS legacy images (Willett et al. 2013). GZ provides quantitative measures describing various different morphologies, allowing us to test both how the bulk morphology (spiral galaxy or elliptical galaxy) and internal features (like spiral arms, or bars) impact the properties of the sample. We use the weighted vote fractions from GZ with redshift debiasing described in Hart et al. (2016). These numbers are referred to as morphological feature likelihoods, denoted by p_{feature} in what follows.

Finally, we make use of the Galaxy Environment for MaNGA (GEMA) Value Added Catalog (version 2.0.2; Argudo-Fernández et al. 2015; Etherington & Thomas 2015; Wang et al. 2016) to investigate both the local density and overdensities of our samples. Out of GEMA, we make use of the following:

- (i) Local_density (from the 14th Header Data Units in the file, or HDU14): the average density of galaxies in a volume out to the fifth nearest neighbour, corrected by mean overdensity using the correction in Etherington & Thomas (2015).
- (ii) Q_{LSS} (in HDU5), which describes the relative tidal forces caused by large-scale structure (LSS) within 1 Mpc (see Argudo-Fernández et al. 2015).

In addition, we calculate a Q parameter (based on that described in Verley et al. 2007) that attempts to quantify the tidal force experienced by a galaxy from its nearest neighbours, within $\Delta V = 500 \text{ km s}^{-1}$ (Garland et al., in preparation).

2.4 Sample and control sample selection

We cross-match the DR17 (v2.7.1) Pipe3D catalogue (Sánchez et al. 2018), the H I-MaNGA DR3 catalogue (Stark et al. 2021), and data from the WISE catalogue for the DR17 sample. We remove any MaNGA bundles that are not galaxies, or are pairs of galaxies, or have DAPQUAL flag set to ‘CRITICAL’, as well as any H I detections that fail the test for possible confusion. This results in a parent sample of 4316 galaxies, out of which 1575 had H I detections and 2741 had H I upper limits.

We define all of these 1575 galaxies detected by H I-MaNGA as ‘H I rich’; detection in H I-MaNGA typically means that they have

²<https://sdss-marvin.readthedocs.io/en/latest/tools/bpt.html>

³<https://wise2.ipac.caltech.edu/docs/release/allwise/>

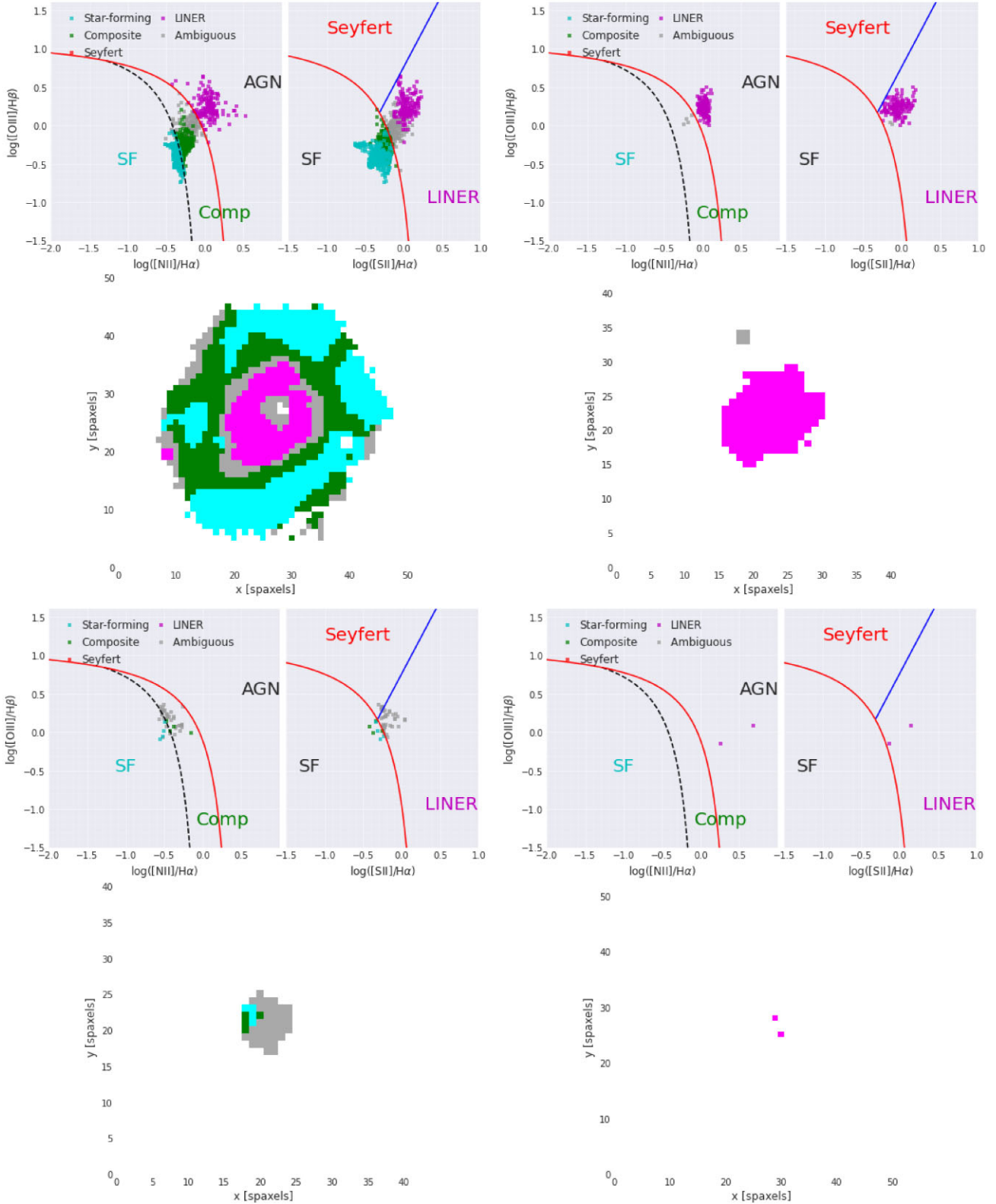


Figure 1. Example BPT diagrams (generated using the MARVIN tool `get_bpt`) of four different galaxies in our H I-rich low-SF sample, illustrating some of our BPT classifications: in cLIER galaxies (example to the top left; plateifu: 8450–6101), the cLIER emission is spatially extended, but accompanied by SF at larger galactocentric distances, while in eLIER galaxies (example to the top right; plateifu: 9090–3702), LIER emission is extended throughout the whole galaxy. We find that our sample of H I-rich low-SF galaxies shows a greater proportion of cLIERs than that found in low H I control (H I-poor galaxies with low SF). Galaxies dominated by ambiguous spaxels (i.e. spaxels that show emission-line ratios with ambiguous BPT classification) were classified as ‘Composite+’ (example to the bottom left; plateifu: 9892–3702) and galaxies with either few emission-line spaxels or spaxels with no clear spatial distributions of classifications were classified as ‘Cannot tell’ (example to the bottom right; plateifu: 9088–6103).

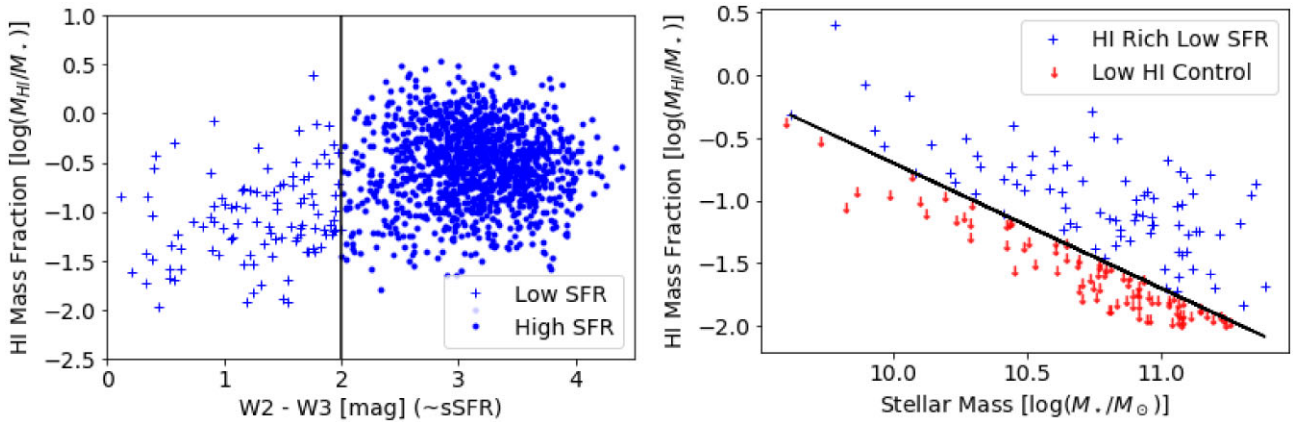


Figure 2. Left: H I mass fraction plotted against W2-W3 from WISE (a colour that correlates well with sSFR). Our prospective sample galaxies are marked with plus sign, while all other H I detections are shown as round points. Right: H I mass fraction versus stellar mass plot for the main sample and the low H I control sample (which are shown plotted at the estimated upper limit of undetectable H I). The diagonal line shows the largest upper limit ($\log M_{\text{HI}}/M_{\odot} < 9.3$) we allow in the low H I control.

an H I mass, $M_{\text{HI}} > 10^9 M_{\odot}$ (Masters et al. 2019; Stark et al. 2021). Note that this sample has stellar masses that range from 10^9 to $10^{11} M_{\odot}$ (see Figs. 2 and 3).

To define high- and low-SFR subsets, we make use of the WISE photometry. We follow Parkash et al. (2019) in assuming that galaxies with a colour $W2-W3 < 2.0$ have an sSFR ($\text{sSFR} = \text{SFR}/M_*$) $< 10^{-10.4} \text{ yr}^{-1}$. Parkash et al. (2019) based this on the W1-W2 stellar mass calibration of Cluver et al. (2014) with the W3-SFR calibration of Brown et al. (2017). We define this to be the limit for the low-sSFR sample. This method is more robust to the effect of dust obscuration than optical or UV measures of SF, although there are some disadvantages to be recalled in interpreting our samples, such as it missing SF in the outer regions of some galaxies, and also cases where the emission from evolved stars can dominate W3 masking the signal of low levels of SF. The left panel of Fig. 2 shows the W2-W3 versus the H I mass fraction for these 1575 galaxies with H I detection. We find that 105 (7 ± 1 per cent) have $W2-W3 < 2.0$. Out of these 105 galaxies, we select the 83 galaxies with $\log M_{\text{HI}}/M_{\odot} > 9.3$ (see right panel of Fig. 2 for reference) as our ‘main sample’ of H I-rich galaxies with low SF. We apply this selection of $\log M_{\text{HI}}/M_{\odot} > 9.3$ in order to ensure that our H I-rich low-SF sample does not share parameter space with H I non-detections in the ‘low H I control’. We note that higher mass galaxies typically have lower sSFRs even when star forming, so a constant cut in sSFR selects low-SF massive galaxies that are somewhat closer to the star-forming population than those among the lower mass galaxies.

In order to understand in which ways the low-SFR H I-rich galaxies differ from more typical galaxies, we create two sets of control samples. Both of them include galaxies that are selected to have a distribution of stellar masses matched with the stellar mass of the main sample. A ‘high SF control’ is selected to have similar H I mass fraction and stellar mass as our main sample, but $W2-W3 > 2.0$ (or $\text{sSFR} > 10^{-10.4} \text{ yr}^{-1}$). A total of 1330 galaxies meet these selections, out of which we find the 83 with closest matches in stellar mass and H I mass fraction to our main sample, without repeating any galaxies. A ‘low H I control’ is selected to have both low SF ($W2-W3 < 2.0$) and similar stellar masses as our main sample, but be H I poor. We use measured upper limits to define this H I-poor comparison set using a threshold of $M_{\text{HI}} < 10^{9.3} M_{\odot}$, which picks out galaxies with low H I mass fractions for their stellar mass (see right panel of Fig. 2). There is some overlap in the H I upper mass limits and some of our

lower mass H I detections; however, overall this selection results in a sample with significantly less H I than our main sample. We find 1400 galaxies meeting these selections, and follow the procedure noted above to find the best possible stellar mass and sSFR (colour) matched sample.

While the statistical rigour of our work could be improved by implementing multiple random draws for these control samples, it is important to realize that even though MaNGA is the largest currently available IFU sample with 10010 galaxies in total, at this time of analysis, the available H I-MaNGA sample contained $N = 6632$ of the full MaNGA sample, which limits the number of possible independent controls to less than 10, even if we allow matches as large as 0.4 dex within the two matched quantities for each control.

Inclination can impact measures of sSFR via dust obscuration (although by using WISE colours we limit this impact). For disc galaxies, axial ratio is a proxy for inclination. We note that we have applied no morphology selection yet, however a check of the distribution of axial ratios for our three samples, finding statistically similar distributions peaking at $b/a = 0.7$, with a hint that the low H I, low SF skews rounded (see Section 3.3 where we discuss how this subset is, perhaps unsurprisingly, less likely to be disc galaxies, so it is reasonable to expect that they appear on average rounder on the sky).

For a comparison of all selection properties of the main sample with both controls, please see Fig. 3, which shows the histograms of W2-W3, stellar mass, and H I mass fraction as well as plots of H I mass fraction against both W2-W3 and stellar mass. The typical properties of galaxies in the three samples are also summarized in Table 1.

3 RESULTS

3.1 Source of ionization

In their analysis of 91 H I galaxies with little or no SF from Parkash et al. (2019) discovered that they had very high LIER fractions and speculated that the presence of H I gas with little/no SF may be a precondition for LIER emission. Looking at the resolved BPT diagrams of the samples from MaNGA, we find that our H I-rich low-SF (main) and low H I control samples both have a high

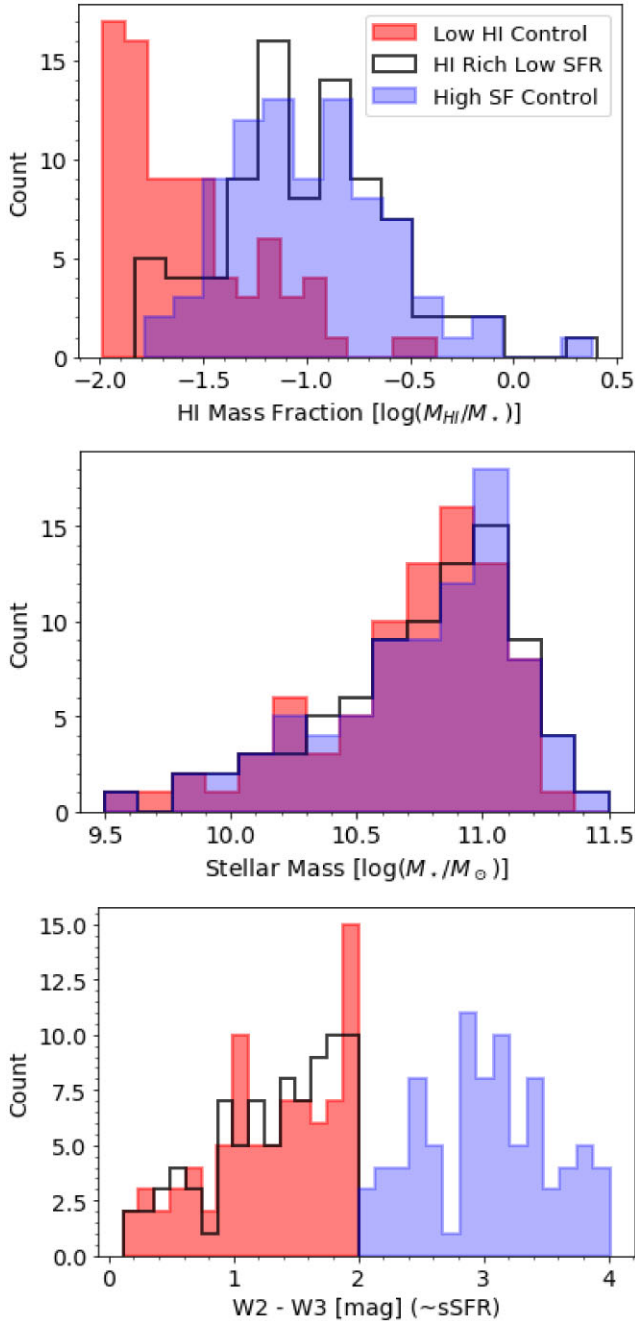


Figure 3. Top: HI mass fraction distribution (we show limits for low HI control). The main sample and HI-rich control have similar HI mass fractions, while the HI control is offset. Centre: the distribution of stellar mass for the main sample and both controls demonstrating how they overlap well. Bottom: the distribution of W2-W3 (as a proxy for sSFR) for all three samples showing the split between high and low SF. See Section 3.2 for p-values comparing these distributions.

proportion of LIERs (77 ± 11 and 60 ± 10 per cent of classifiable maps, respectively). In contrast, the high SF control was found to have relatively low proportion of LIERs (19 ± 5 per cent of classifiable maps). We thus conclude that in our samples, the high LIER fraction correlates with low SFR, not requiring a combination of low SFR and HI content.

We further categorize LIER emission based on its spatial distribution, following the definitions of Belfiore et al. (2016, see

Table 1. Summary of main sample and both control samples. All have $N = 83$ galaxies. sSFR limits are based on W2-W3 colours.

Sample	M_{HI} (M_\odot)	sSFR (yr^{-1})	$\langle \log M_*/M_\odot \rangle$
Main sample (HI rich, low sSFR)	$> 10^{9.3}$	$< 10^{-10.4}$	10.76
High SF control (HI rich, high sSFR)	$> 10^{9.3}$	$> 10^{-10.4}$	10.76
Low HI control (HI poor, low sSFR)	$< 10^{9.3}$	$< 10^{-10.4}$	10.72

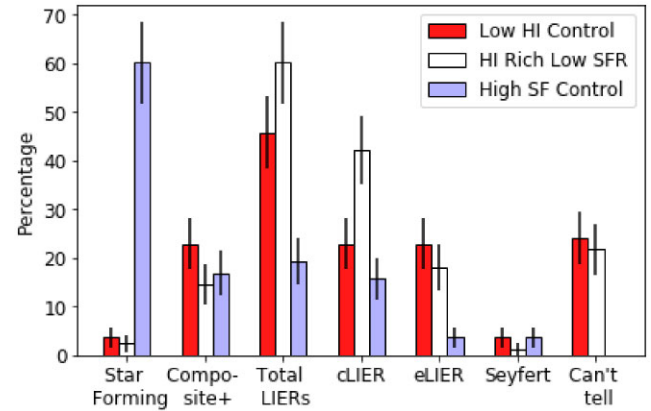


Figure 4. Bar graph showing the primary ionization map category of each of the three samples expressed as a percentage. It is clear that both low-SFR samples, regardless of HI status, have high LIER fractions.

Table 2. Summary of resolved BPT classifications. Columns show total numbers, and percentages relative to the number of classifiable maps, with Poisson counting errors.

Classification	HI-rich low-SF sample	High SF control	Low HI control
SF	2 (3 ± 2 per cent)	50 (60 ± 9 per cent)	3 (5 ± 3 per cent)
Composite+	12 (19 ± 5 per cent)	14 (17 ± 5 per cent)	19 (30 ± 7 per cent)
Total LIERs	50 (77 ± 11 per cent)	16 (19 ± 5 per cent)	38 (60 ± 10 per cent)
cLIERs	35 ($70^a \pm 12$ per cent)	13 ($81^a \pm 23$ per cent)	19 ($50^a \pm 12$ per cent)
eLIERs	15 ($30^a \pm 8$ per cent)	3 ($19^a \pm 11$ per cent)	19 ($50^a \pm 12$ per cent)
Seyfert	1 (2 ± 2 per cent)	3 (4 ± 2 per cent)	3 (5 ± 3 per cent)
Classifiable	65 ($78^b \pm 10$ per cent)	83 ($100^b \pm 11$ per cent)	63 ($76^b \pm 10$ per cent)
Cannot tell	18 ($22^b \pm 5$ per cent)	0 ($0^b \pm 0$ per cent)	20 ($24^b \pm 5$ per cent)

^aThe per cent relative to all LIERs rather than all maps.

^bThe per cent relative to sample size rather than classifiable maps.

Section 3.1 where we describe this in more detail). Fig. 4 shows a visualization of the primary ionization category based on the resolved BPT diagrams; numbers are given in Table 2. In cLIER galaxies (for an example, see the upper left panel of Fig. 1), the cLIER emission is compact, but typically larger than the PSF and is accompanied by SF at larger galactocentric distances, while in eLIER galaxies (example in the upper right panel of Fig. 1), LIER emission is extended throughout the whole galaxy. Among the LIERs, while we found an equal proportion of cLIERs (50 ± 11.5 per cent) and eLIERs (50 ± 11.5 per cent) in the low HI control, LIERs in both the main sample and high SF control are skewed heavily towards cLIERs (70 ± 12 and 81 ± 23 per cent, respectively) compared to eLIERs (30 ± 8 and 19 ± 11 per cent, respectively). This implies that while overall the presence of LIER emission is tied to low SFR (regardless of HI content), cLIER emission also favours high HI content (regardless of global SF). This excess of cLIERs could be a

feature of our W2-W3 based selection for low-SF galaxies – which is dominated by a central old stellar population, may still be surrounded by an extended SF disc. Further analysis of the UV of these samples would be interesting.

AGN feedback has been of significant interest in the extragalactic community as a potential cause of quenching for some years (e.g. Fabian 2012; Heckman & Best 2014; Xu et al. 2022b). While there is no clear result on links to AGN from the BPT analysis, another approach to determining whether AGN feedback may be directly influencing gas disc stability (i.e. preventing the cold gas in our main sample from forming stars) is via direct detection of winds or jets from galactic nuclei. Radio-mode feedback provides one avenue for stabilizing gas discs against collapse and SF. We cross-match the three samples with the Faint Images of the Radio Sky at Twenty-cm (FIRST) survey (Becker, White & Helfand 1995) to search for radio-loud AGN. Using a sky position match within 10 arcsec, we find that just 2 of the main sample are detected in FIRST, while 10 of the low H I control are detected and 16 of the high-SF H I-rich control. This analysis does not provide support for AGN feedback being the reason our H I-rich main sample has usually low SFR.

Radio-quiet AGN may be another avenue for suppressing collapse in gas discs, but detecting these AGNs would require a stacking analysis (e.g. Roy et al. 2018) that we do not perform here. However, another direct AGN signature that has been studied for MaNGA galaxies is ‘red geysers’ (Cheung et al. 2016), a subset of galaxies with evidence of biconical outflows in spatially resolved H α equivalent width maps. Further analysis of a larger sample by Roy et al. (2018) confirmed enhanced nuclear radio emission from red geysers consistent with weak AGN activity, suggesting that red geysers are another manifestation of radio-quiet AGN feedback. Frank et al. (2023) explored whether red geysers are preferentially more gas rich than other quiescent galaxies and found tentative evidence for a slight gas fraction enhancement, but not at a statistically significant level, making it unclear whether outflows are truly stabilizing gas effectively.

Using existing red geysers classifications, we explore whether they are preferentially found in our gas-rich, non-star-forming main sample. Red geysers, by their definition (being in red/low-SF galaxies) are only identifiable in our main sample, and low H I control (as the high SF control is composed of star-forming galaxies that are almost all blue). We restrict this check to red galaxies with Near-Ultraviolet (NUV) colors, $\text{NUV}-r > 5$ and MPL-9 where red geysers are identified, which excludes the entire H I-rich control sample. We find that 3/25 and 7/42 of the galaxies in our main and low H I control samples are red geysers. The 95 per cent binomial confidence intervals on the fraction of red geysers are 0.04–0.30 and 0.08–0.31 for the main and low H I control samples, respectively. Therefore, while there is a suggestion that we find fewer red geysers in the main sample compared to the low H I control, this is not statistically significant, and is definitely not providing evidence of an excess of red geysers among H I-rich low-SF galaxies contributing to the suppression of SF, but rather perhaps a role in red geysers removing any H I gas that is present.

3.2 Rotational motion and velocity dispersion

It is interesting to consider whether the stars and gas in our H I-rich low-SF galaxies have similar motions to the control samples. We make histograms of both the H α and stellar velocity dispersion, rotation widths, and asymmetry (defined as the difference between HI_CLIP and LO_CLIP on both sides); all are taken directly from the DAP and measured within $1r_e$. The histograms are presented

in Fig. 5, while p-values from the Kolmogorov–Smirnov (KS) tests⁴ comparing the main sample and the two controls are given in Table 3.

For H α velocity measures, we only show galaxies with a median H α surface brightness within $1r_e$ of more than $0.3 \times 10^{-17} \text{ erg s}^{-1} \text{ cm}^{-2} \text{ spaxel}^{-1}$. This was an empirically determined limit, which resulted in reliable velocity measures from a well-detected line across enough of the IFU that the velocity field was classifiable. This removes 17 galaxies from the main sample, and 15 from the low H I control (all of the H α maps from high SF control meet this criteria).

We find that there are statistically significant ($p < 0.05$) differences between the main sample and the low H I control in all three H α velocity measures – rotation speed, velocity asymmetry, and velocity dispersion. In all three, the low H I control skews to larger values, possibly revealing a high outflow fraction caused by red geysers, or other non-rotational motion of the H α gas (in the previous section, we demonstrated that the low H I control sample has a slight excess of red geysers, and a defining feature of red geysers is their high gas velocity dispersion; Roy et al. 2018).

While the H α mean rotation and asymmetry are similar between the main sample and its high SF control, we do find a significant difference in gas velocity dispersion, such that the high SF control typically has lower gas dispersions, consistent with the H α gas being more settled in this control sample.

For the stellar velocity fields, we find that the only statistically significant difference is in stellar velocity dispersion between the main and high SF control samples, where we see a shift to larger velocity dispersions in the main sample relative to the high SF control. Again, we find a picture where the high SF control shows evidence for more settled disc-like behaviour than the main sample. There is a hint that the low H I control has even higher stellar velocity dispersion, but this is not a statistically significant difference ($p = 0.717$).

For the two H I detected samples, we can also compare the H I rotation widths, corrected for inclination following the method described in Masters et al. (2019). No notable difference is seen (see Fig. 6).

3.2.1 Kinematic misalignment

One of the cleanest tracers of external processes impacting galaxies is the signature of kinematic misalignment between stars and gas. Gas is likely to enter a galaxy from its local environment at a random angle relative to the rotation axis of any existing stars and gas, and therefore can set up kinematically distinct components. Visually inspecting the H α and stellar velocity fields for all galaxies in the main and control samples, we find a noticeable enhancement in the fraction of kinematic misalignment between gas and stars in our main sample of H I-rich, but not star-forming galaxies. This is a subjective measure of kinematic asymmetry, but the enhancement is so large that a more quantitative method is unlikely to change our result. An example of a kinematically misaligned galaxy is shown in Fig. 7. Overall, we find that 10 ± 3 per cent of galaxies with both stellar and gas velocity fields well measured (or 8 per cent of all H I-rich, low-SF galaxies) have evidence of what are plausibly counter-rotating components, and another 10 per cent show kinematic offsets. This adds up to 20 per cent (18 per cent of the sample) showing clear evidence of kinematic misalignment

⁴KS tests performed using the SCIPY stats KS two-sample test package, https://docs.scipy.org/doc/scipy/reference/generated/scipy.stats.ks_2samp.html.

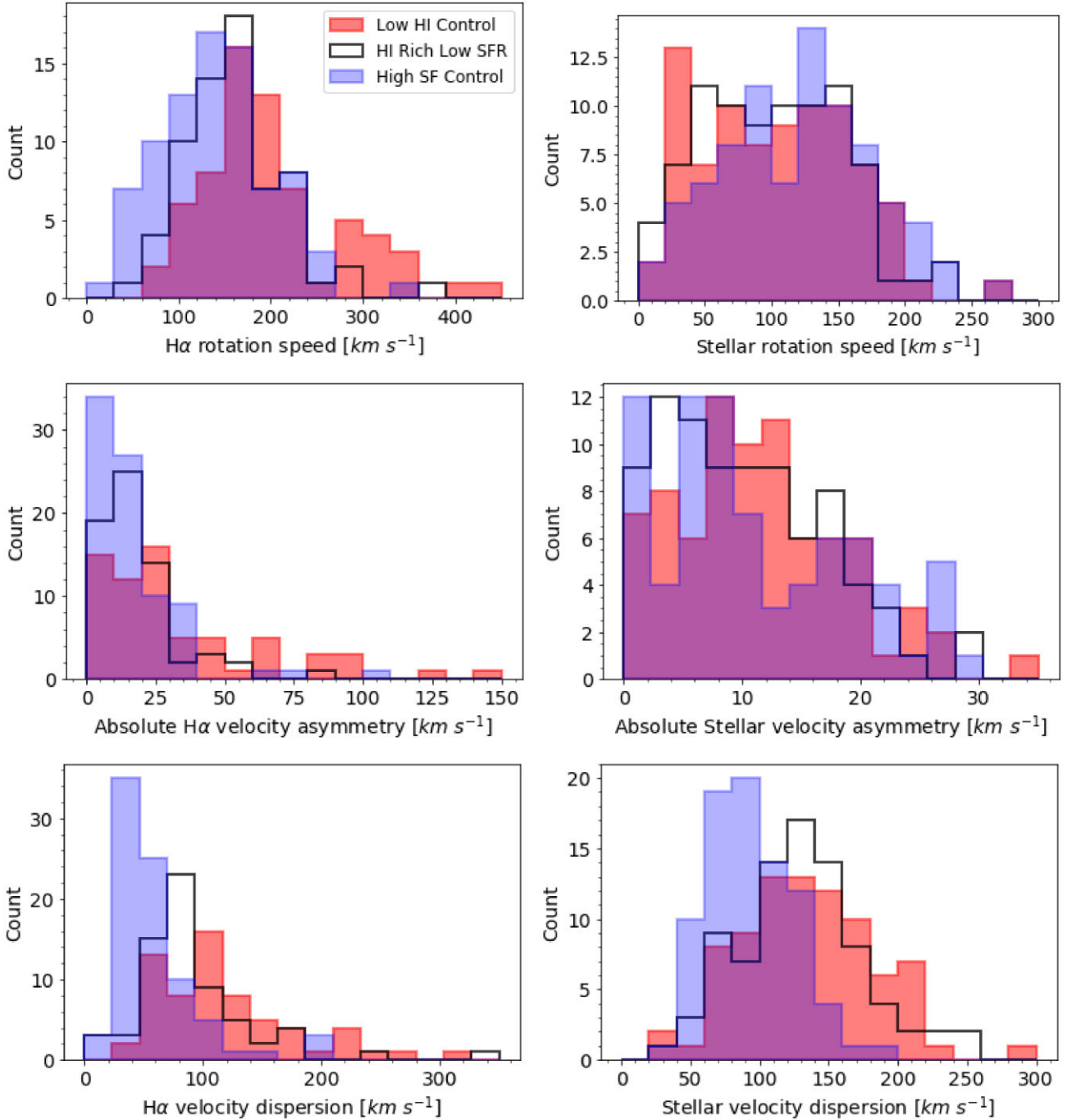


Figure 5. Distribution of properties measured from the H α velocity (left column) and stellar velocity (right column) fields. From top to bottom, we show the bulk rotation, absolute asymmetry, and velocity dispersion. The main sample skews to larger values in all H α kinematics measures relative to the low H I control and also skews higher in the H α and stellar velocity dispersions, relative to the high SF control (see Table 3 for p-values).

between gas and stars. The frequency of kinematic offset appears similar in the low H I control sample (10 per cent), but there are just three galaxies showing clear evidence of what might be counter-rotation in this sample. In the star-forming control sample, we find no counter-rotators, and only one galaxy with evidence of any kind of kinematic offsets. This is a really notable difference between our sample and the controls and overall is a high fraction of kinematic misalignment. For a summary of these numbers, see Table 4. One caveat to note is that we see a similar fraction

of red geysers in our main sample of H I-rich low-SF galaxies (4 ± 2 per cent) and low H I control samples (8 ± 3 per cent), so some of the gas velocities seen in the maps are plausibly outflows driven by the red geysers, rather than kinematic misalignment driven by gas inflow. No red geysers are detected in our high SF control (by definition, red geysers are only possible to identify in low-SF samples).

In the Jin et al. (2016) analysis of the first year of MaNGA data, they find that 5 per cent (66/1351) of the sample show kinematic

Table 3. KS p-values for comparison of all histograms in all figures in this paper. Values that reveal significant differences ($p < 0.05$) between the main sample and the controls are bolded. The figure to which each row refers is given in the final column.

Parameter	High SF control	Low H I control	Figure
Stellar mass	0.998	0.586	Fig. 3
H I mass fraction	0.998	0.000	Fig. 3
W2-W3 (\sim sSFR)	0.000	0.998	Fig. 3
H α rotation speed	0.170	0.004	Fig. 5
Absolute H α velocity asymmetry	0.321	0.002	Fig. 5
H α velocity dispersion (HA.SIGMA.1RE)	0.000	0.000	Fig. 5
Stellar rotation speed	0.133	0.932	Fig. 5
Absolute stellar velocity asymmetry	0.091	0.353	Fig. 5
Stellar velocity dispersion (STELLAR.SIGMA.1RE)	0.000	0.717	Fig. 5
H I line width	0.586	–	Fig. 6
Disc galaxy or smooth (early type)? (t01_smooth_or_features_a02_or_disk_debiased)	0.018	0.001	Fig. 8
Bulge size score	0.006	0.053	Fig. 8
Visible spiral arms (t04_spiral_a08_spiral_debiased)	0.015	0.001	Fig. 8
Presence of a bar (t03_bar_a06_bar_debiased)	0.032	0.147	Fig. 8
Metallicity ($12 + \log(O/H)$)	0.040	0.189	Fig. 9
Tidal force from nearest neighbour, Q	0.961	0.033	Fig. 9
Tidal force from local environment, Q_{LSS}	0.586	0.006	Fig. 9
Local overdensity	0.793	0.383	Fig. 9

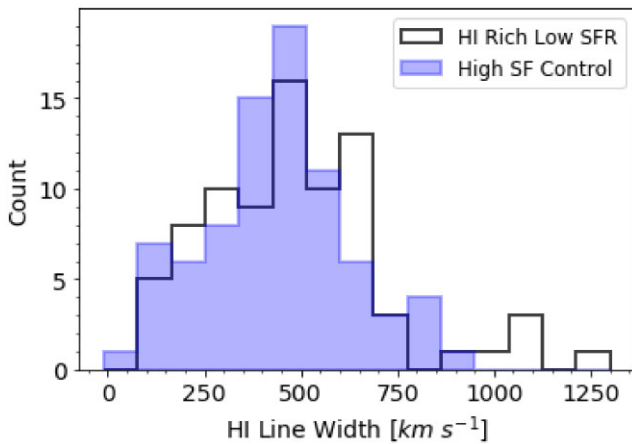


Figure 6. The distribution of inclination corrected H I line widths (in km s^{-1}) for galaxies in the main sample and high SF control (i.e. the two subsamples in which H I is detected). There is no statistically significant difference between these (see Table 3 for p-values).

misalignment. Xu et al. (2022a) recently updated this work to make use of the almost complete MaNGA sample, MPL-10, finding a similar overall fraction of 4.8 per cent or 456/9546 galaxies with kinematic misalignment. In Jin et al. (2016), they also show how the misaligned fractions vary as a function of stellar mass and SFR properties. They find that the fraction of kinematic misalignment peaks (at around 10 per cent) at $\log M_*/M_\odot = 10.5\text{--}11.0$. The median stellar mass of our sample is $\log M_*/M_\odot = 10.85$ right in this peak (recall that all our samples are arranged to have matching stellar mass distributions). They also find that misalignment is more common in more weakly SF galaxies. The upper sSFR limit for our low-SF main and control samples is roughly $\log(\text{sSFR yr}) < -10.4$, which is the lowest sSFR bin considered in Jin et al. (2016), where they

find misaligned fractions of 15–30 per cent. They do not investigate the cold gas properties of their sample; however, it appears that our main sample has fractions of kinematic misalignment consistent with other low-SF samples of this mass. Even with this, there is still perhaps evidence of a higher counter-rotating fraction than typical.

3.3 Morphology

The morphology of a galaxy is another way to trace its kinematics, and/or look for differences in the assembly history (bulge-dominated galaxies being more likely to have had significant mergers in the past). We made use of a catalogue of morphologies of MaNGA galaxies, which was released in the SDSS-IV DR16. These morphologies are mostly from Galaxy Zoo 2 (GZ2; Willett et al. 2013; Hart et al. 2016), with some additional classification of MaNGA sample galaxies, which were missing in GZ2. We identify spiral galaxies, using a selection of $p_{\text{features}} > 0.5$.⁵ An additional cut of $b/a > 0.3$ is used to exclude very edge on disc galaxies, so that we can make use of bar and spiral arm identifications in the remaining subset.⁶ We calculate the bulge size of these galaxies using equation (4) of Masters et al. (2019), which makes use of the consensus answers about bulge size in GZ.

Using GZ gives us continuous variables for all these morphologies, so we can make a comparison of the distribution of these morphological properties in the three samples (see Fig. 8, with p-values for KS tests comparing the distributions in Table 3).

We find that our main sample contains galaxies which are morphologically different to those in both the high SF and low H I controls.

⁵Here, p_{features} is short for t01_smooth_or_features_a02_features_or_disk_debiased.

⁶Bar and spiral votes from t03_bar_a06_bar_debiased and t04_spiral_a08_spiral_debiased, respectively.

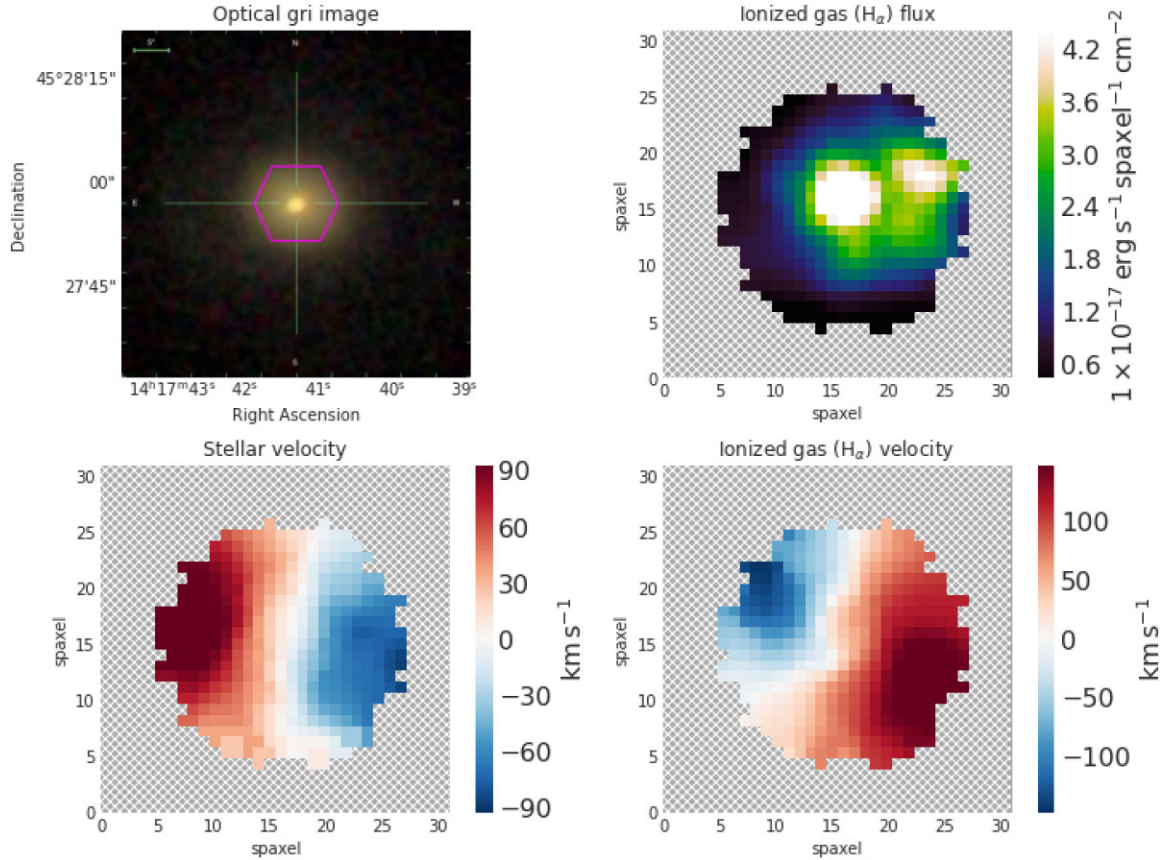


Figure 7. A set of example MaNGA maps showing a counter-rotating galaxy (plateifu: 8329–1901) from H I-rich low-SF sample. Panels show the optical gri image (upper left) with the purple hexagon indicating the region covered by the MaNGA bundle; the H α flux (upper right) in MaNGA data with the colour bar giving the scale and units; and stellar and H α velocity maps (lower left and right, respectively) with the colour bars showing the scale in km s^{-1} relative to the central velocity of the galaxy. The gas rotates in the opposite sense to the stars.

Table 4. Kinematic misalignment fractions. All errors are 1–3 per cent for these sample sizes. The range of fractions indicates comparison with the entire sample, or the subset with H α detections.

Parameter	H I-rich low-SF sample	High SF control	Low H I control
H α detected	72 (87 per cent)	83 (100 per cent)	74 (90 per cent)
Counter-rotating	7 (8–10 per cent)	0 (0 per cent)	3 (4 per cent)
Offset rotation	8 (10–11 per cent)	1 (1 per cent)	8 (10–11 per cent)

The high SF control population is more likely to contain galaxies classified as a disc galaxy, with a smaller bulge, less visible bars, and more visible spiral arms than galaxies in the main sample. Galaxies in the low H I control are more likely to be classified as smooth, and if features are seen in galaxies in this control it is less likely that they are spiral arms than features seen in galaxies in the main sample.

Bars have previously been associated with low-SF disc galaxies (Masters et al. 2011) as well as disc galaxies with lower than average H I content (Masters et al. 2012). We find a slight, but statistically significant enhancement of bars in our sample over the high SF control, while the low H I control and the main sample appear to have similar likelihood of hosting a visible bar. Overall 44 ± 9 per cent of the main sample have a strong bar ($p_{\text{bar}} > 0.5$ as defined in Masters et al. 2011), while just 29 ± 8 per cent of the high SF control sample host strong bars.

Overall, it appears that the presence (or absence) of spiral arms may be the most important feature. Our H I-rich low-SF main sample

is found to be less likely to have very obvious arms than the high SF control. Although it is true that both samples have the majority of galaxies in the $p_{\text{spiral}} = 1$ bin, they are statistically different, as the main sample has more intermediate values of p_{spiral} and more galaxies in the $p_{\text{spiral}} = 0$ bin than the high SF control. This is interesting as spiral arms have been invoked as a way to trigger SF (e.g. see Sellwood & Masters 2022 for a recent review), although spirals may also be more visible in a disc with significant population of younger stars. Our main sample is also more likely to have visible spiral arms than the low H I control.

3.4 Metallicity

The gas phase metallicity provides a trace of how pristine the interstellar medium (ISM) is in these galaxies. We made use of MaNGA spectra along with equation (5) of Kewley & Dopita (2002) to calculate the average gas metallicity of galaxies in our samples within $1r_c$ and consider whether there are differences (see the upper left panel of Fig. 9 and Table 3). The distributions of gas phase metallicity are found to be indistinguishable between the main (H I rich low SF) and low H I control while differing only slightly between the main and the high SF control sample. However, while statistically significant, the difference with the high SF control is small and median values agree within the standard deviation. This is not a clear signal of the physical origin of the H I-rich low-SF galaxies, but is suggestive of their formation from galaxies that could be in the

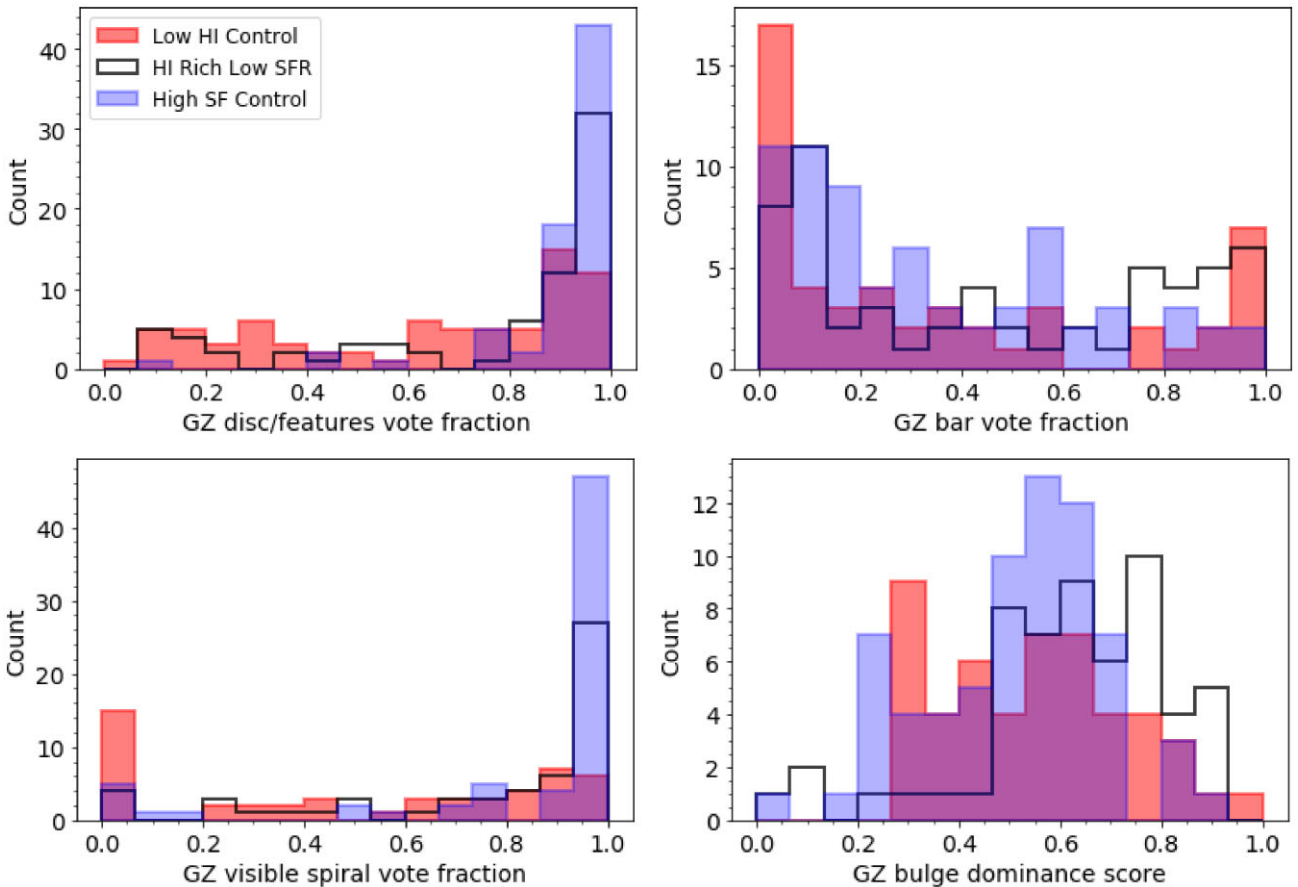


Figure 8. Histograms of morphological feature likelihoods from GZ debiased and weighted vote fractions for the three samples. Top left: histogram of (debiased) votes for visible disc/features showing how the main sample has more discs than the low H I control, but fewer than the high SF control. Top right: for face-on disc galaxies, a histogram of (debiased) votes for a visible bar or (lower left) visible spirals. Lower right: a bulge size comparison (based on votes for bulge size – see text for details). The high SF control is distinct in having both more spirals and smaller bulges than the main sample. The low H I control has notably fewer visible spirals. Our H I-rich low-SF main sample also has significantly more visible bars than the high SF control.

low H I control with the addition of pristine gas, which has not yet contributed to SF, so the gas phase metallicities have not yet changed.

One caveat to note here is that we use the Kewley & Dopita (2002) prescription, which is based on an assumption of SF ionization to calculate metallicity for all spaxels, not just those with ionization from SF. As discussed in Section 3.1, the different samples do have different amounts of non-SF-based ionization. However, our use of $[\text{N II}]/[\text{O II}]$ to estimate metallicity largely minimizes bias due to the fact that nitrogen and oxygen have very similar ionization energies, making their ratio highly insensitive to ionization parameter and the hardness of the ionizing spectrum (Kewley & Dopita 2002; Zhang et al. 2017). Therefore, we apply the same prescription on all spaxels regardless of whether they are primarily ionized by SF.

3.5 Environment

Finally, since environment is known to be important in galaxy evolution (e.g. Peng et al. 2010), we make use of a variety of environment measures to investigate both the local density and overdensities of our samples.

We consider three measures of environment at different scales: a local overdensity (to the fifth nearest neighbour); tidal forces generated by LSSs, Q_{LSS} ; and tidal forces from the nearest neigh-

bouring galaxy, Q (see Section 2.3 for more on all of these). Histograms of these values for all samples are shown in Fig. 9, Table 3 for KS p-values for the comparisons. We find a statistically significant difference in tidal forces (from both the LSS and the nearest neighbour) between the main sample and low H I control, such that the low H I control galaxies are more likely to be found in regions with higher tidal forces (larger values of Q and Q_{LSS}). This control also appears to skew to higher local density values (although this difference is not found to be statistically significant). No difference is found in the environments of the main sample and high SF control.

4 DISCUSSION

Our sample of unusual H I-rich, yet low-SF galaxies is a significant outlier in the typical H I detected galaxy population, comprising just 5 ± 1 per cent of H I detected galaxies. Studying them in comparison to more typical galaxies (H I rich and high SF, or H I poor and low SF) allows us to consider the evidence for or against likely physical origins of this subset of galaxies, which initially appeared to present interesting case studies for how quenching may occur in the galaxy population.

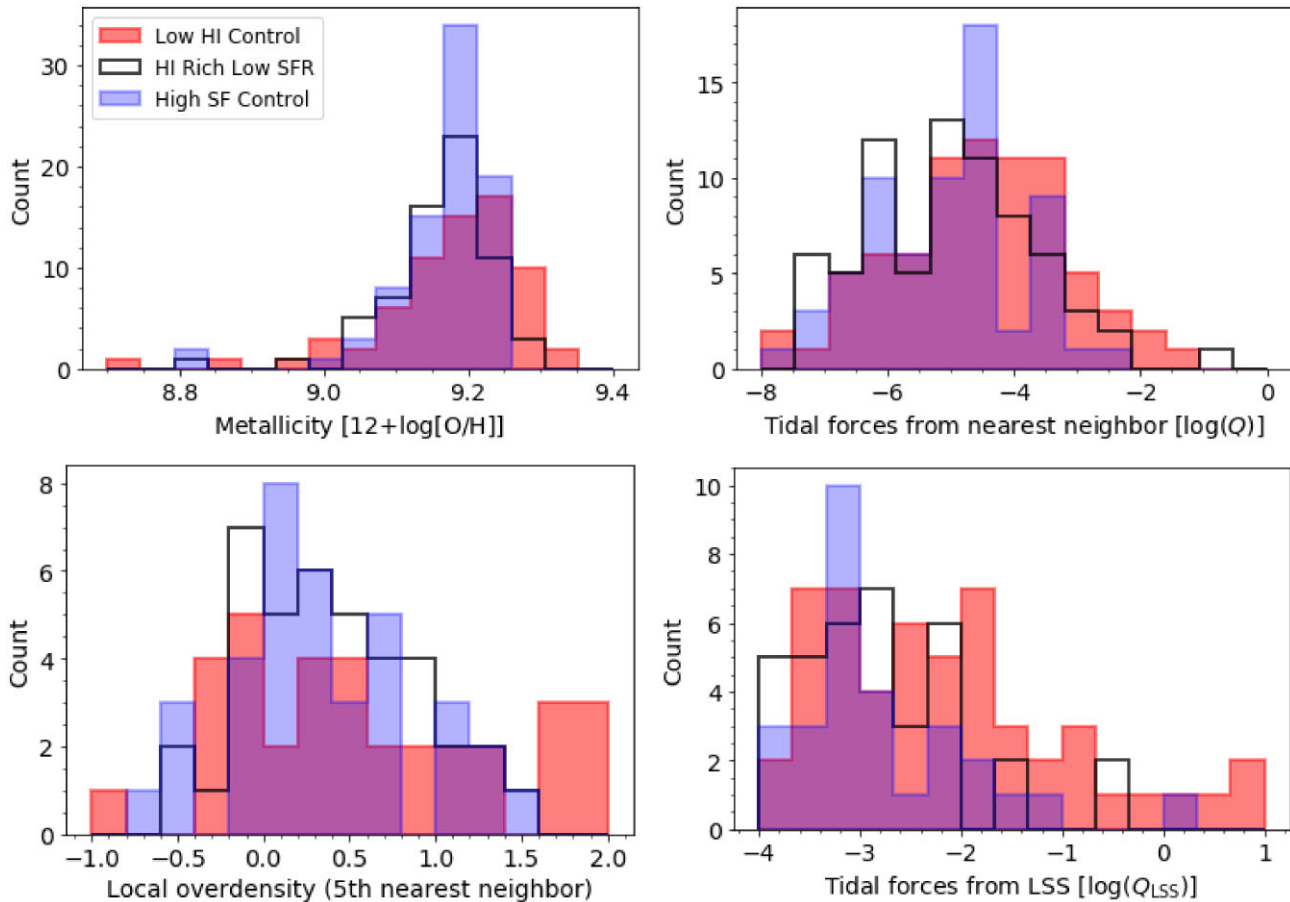


Figure 9. Histograms of the distribution of metallicity (upper left), tidal force from the nearest neighbour, Q (upper right on a log scale), local overdensity (to the fifth nearest neighbour, lower left), and tidal force from all nearby neighbours within 1 Mpc, Q_{LSS} (lower right) for all samples (see Section 2.3 for more on these). The tidal force parameters are unitless; larger values correspond to stronger tidal forces. We find statistically different distribution of metallicity between the main and high SF control. For the tidal force-based environment measures (Q and Q_{LSS}), only the distributions between the low HI control and main sample are statistically different (see Table 3 for p-values).

Since we typically expect a strong correlation between HI content and SF (e.g. Saintonge et al. 2016), galaxies that are HI rich but lacking significant SF must therefore have experienced/be experiencing the following:

- (i) Recent accretion of HI gas (not yet impacting SF).
- (ii) Heating of gas from feedback mechanisms blocking all or part of the $H\text{I} \rightarrow H_2 \rightarrow \text{SF}$ pipeline.
- (iii) Some other process preventing or significantly slowing the cooling of the HI gas.

In the case of recent accretion (i), we expect that the main sample would be closest in properties to the low HI control, just with the addition of HI. In addition, we might expect to see (a) lower metallicities in the gas in the main sample relative to the low HI control and (b) an increase in the fraction of the main sample found in environments where there is more access to gas infall, greater disturbance in the $H\alpha$, or other gas velocity disturbances (e.g. counter-rotation). There is no statistically significant evidence that the gas phase metallicity of the main sample is lower than that of the low HI control; however, the histogram of metallicity values in the low HI control visually looks skewed to higher metallicities (Fig. 9). A future analysis with a larger sample size may reveal slight differences in the distribution (or confirm their similarity). There is a weak statistically significant correlation with environment measures

– the main sample is likely to be in lower density environments than the low HI control (Fig. 9), where they may have better access to material for cold flow accretion.

Perhaps most convincing as evidence of possible gas infall in the sample, there is a significant increase in the observed fraction of counter-rotation and kinematic offsets in our sample, suggesting that a recent gas accretion origin is plausible. For example, Starkenburg et al. (2019) use Illustris to consider the origin of galaxies with counter-rotation between stars and gas and suggest that it requires gas infall on to a gas-poor galaxy – explaining why galaxies with earlier type morphologies and lower SF tend to more often show counter-rotation. Both Bryant et al. (2019) and Ristea et al. (2022) find evidence that supports this model from samples of kinematically misaligned galaxies in the SAMI (Sydney-Australian-Astronomical-Observatory Multi-object Integral-Field Spectrograph) galaxy survey. Rathore et al. (2022) and Zhou et al. (2023) use MaNGA data to point to evidence that this kind of misaligned gas accretion is a formation mechanism for S0 galaxies and/or causing rejuvenation of SF in previously quiescent S0s. These ideas are consistent with us catching a sample at the early stages of cold gas infall on to a previously gas-poor population. However, there is no observable difference in the dynamical properties of the HI (see Fig. 6), which therefore appears to have had time to settle normally. There are a lot of open questions about what sets the rate of cool gas accretion on

to galaxies, and factors that may influence this, including halo mass (e.g. White & Rees 1978), AGN activity (Zinger et al. 2020), LSS environment (Liao & Gao 2019), and even potentially the cosmic ray environment of the galaxies (Butsky et al. 2020).

If the H I in our main sample does not represent recent gas infall, but rather some process blocking the gas-to-stars pipeline, via either heating (ii) or prevention of collapse/cooling (iii), there are multiple ways this can proceed including both internal and/or external processes. For example, cold gas can be heated, or prevented from cooling, further by the following:

- (i) AGN feedback (perhaps revealed via cLIERS).
- (ii) Supernova (SN) feedback, or other ionization from old stellar populations (which may be revealed in eLIERS).
- (iii) Dynamical heating via shocks (e.g. from bars, tidal interactions, and counter-rotation).
- (iv) Larger than typical dark matter fractions (i.e. halo heating).
- (v) Being distributed in a very low density/high angular momentum gas disc.

The latter model (of a high angular momentum, low-density disc) has previously been used to explain large H I content in quiescent discs. For example, Zhang et al. (2019) found surprisingly large H I content in their sample of massive ($M_* > 10^{9.5} M_\odot$) quiescent disc galaxies. They suggest that it is remnant outer, high angular momentum H I, which has a long time-scale to migrate inwards in the absence of perturbations (although as we previously noted, Cortese et al. (2020) suggest that this may be due to them underestimating the amount of extended SF in massive H I discs). Lemonias et al. (2014) obtained resolved H I maps of 20 massive, quiescent galaxies with large H I masses, finding the H I distributed at unusually large radii, suggesting that low sSFRs may be caused by the low-H I gas surface densities in the large H I discs. The H I-MaNGA data are unresolved, so we have no way of obtaining the radial distribution of the H I. The sample investigated here may therefore be an interesting one to follow up with resolved H I imaging in the future. Another interesting follow-up project would be looking at the UV extent of our H I-rich low-SF galaxies to search for low-level extended SF in the low-density disc. Extended UV discs have been observed to correlate well with large H I discs, and have previously been found in nearby galaxies (Thilker et al. 2010; Cortese et al. 2012).

If the main sample galaxies are experiencing feedback heating the gas, or preventing it from cooling, we might expect the process to reveal itself in how that sample differs from the normal high H I, high SF control.

Considering the evidence for AGN feedback in our sample, we do see that about 4 per cent of our main sample (and 8 per cent of low H I control) host red geysers, and the cLIER fraction in the main sample is higher than that in the high SF control (see Section 3.1). The large rates of kinematic misalignment (Section 3.2.1) also could point in this direction, revealing the presence of gas outflows. Linking the two, Duckworth et al. (2020) presented mock MaNGA data based on galaxies in Illustris, and showed that those with kinematic misalignment also typically had enhanced black hole growth and AGN activity.

When considering SN feedback, or ionization from old stars, the high SF control is found to host smaller fraction of eLIERS (Section 3.1), compared to the main sample. So, this process seems plausible. However, we have not quantified the impact of the ionization from SF hiding the signature of eLIERS in the high SF control, and the low H I control has similar fractions of both kinds of LIERS to the main sample.

Dynamical heating of some kind seems to fit the evidence reasonably well, particularly given the high fractions of kinematic disturbance seen in the main sample compared to the high SF control (Section 3.2.1). In contrast, we see little difference in the environments of those two samples, no evidence for larger dynamical masses or halo masses (given the match on stellar mass and rotation widths), but there is evidence for a higher bar fraction (Section 3.3) in the main sample, which could cause shocks via radial flows.

The main sample has less visible spiral arms than the high SF control (Section 3.3), but this could be because spiral arms are enhanced by the presence of the SF more than that the lack of them inhibits SF. It also has more visible bars, particularly strong bars, than the high SF control, consistent with prior work that has associated low SF, in H I-rich galaxies, with the presence of bars (Masters et al. 2011, 2012); however, not all of the main sample has a bar, so this could only explain part of the sample.

Overall, it seems that the sample is consistent with perhaps having some higher than typical recent cold gas infall, but could also be consistent with the presence of H I at large radii where it has been unable to cool. There is some evidence for an excess of AGN and/or other gas ionization, which might additionally be blocking the gas-to-stars pipeline. There is no clear single explanation why all galaxies in the sample selected are H I rich but have low SF, which supports a picture in which all of the possible processes could be happening in some part of the sample. Curiously, Hallenbeck et al. (2014, 2016), who studied very H I-rich galaxies with typical SFR for their (high) stellar masses in the HighMass sample, also concluded that different formation processes were needed to explain these galaxies – citing either recent accretion or unusually high angular momentum in the H I disc.

5 CONCLUSIONS

We study an unusual subset of MaNGA sample galaxies that are found to be H I detections while having very low sSFR. These galaxies represent just 5 per cent of the H I detections of MaNGA galaxies in the large H I follow-up programme for MaNGA (Masters et al. 2019; Stark et al. 2021). We construct control samples consisting of either low-H I low-SFR or H I-rich high-SF galaxies, selected to have matching stellar mass distributions to the main sample in order to investigate the physical processes preventing SF from occurring.

As was previously found by Parkash et al. (2019), H I-rich galaxies with low SF were found to have a significant proportion of LIERS in the MaNGA data. However, unlike Parkash et al. (2019), we find that our control sample of low H I with low SFR has a similarly high fraction of LIERS. This suggests that LIERS are specific to galaxies with low SFR, not necessarily high H I content.

The availability of MaNGA data enables an investigation of spatially resolved BPT diagrams. Following Belfiore et al. (2016), LIERS were further categorized into eLIER and cLIER. The main, H I-rich low-SF sample was found to have a moderately high proportion of cLIERS (70 per cent) more comparable to high SF control (81 per cent) than low H I control (50 per cent). Based on these results, we conclude that cLIER emission also favours high H I content (regardless of global SF).

MaNGA also provides velocity maps, both for stars and for gas. We are only able to use H α velocity maps for well-detected H α emission, but we find that the main, H I-rich low-SF sample has a higher H α velocity width, asymmetry, and dispersion than the low H I control, as well as higher velocity dispersion when compared to the high SF control. The stellar velocity maps are much more similar

between the three subsamples, with a difference only seen in the stellar velocity dispersion between the main and high SF control.

One of the most notable differences between the main sample and the two controls is found in evidence of kinematic misalignment. We find that about a fifth of the galaxies in the main sample with both stellar and gas velocity maps show evidence for either counter-rotation or kinematic misalignment. The low H I control shows a similar but smaller fraction of misalignment, but fewer counter-rotating galaxies, while the high SF control shows much more regular velocity.

We also consider morphology, finding that the main sample is intermediate between the high SF control (more discs/spirals) and the low H I control (more smooth galaxies). The high SF control has much more visible spiral arms, and is less likely to host a strong bar than the main sample.

We look at metallicity, seeing no clear evidence of any significant difference with either control. This suggests that if the main sample form from ‘low H I control-like’ galaxies by infall of pristine gas, this gas has not yet participated in enough SF to enrich the ISM.

Finally, we look at the environments of the three samples, using three different measures of environment on scales from the very local (nearest neighbour) to more LSS. No differences are found in the distribution of environments for the main and high SF control, while we find that the low H I control is slightly more likely to be found in higher density regions, perhaps more separated from intragalactic material available for cold flow accretion than the main sample.

We consider how these observations comparing the main sample with the two controls support various physical processes that could explain these unusual galaxies (Section 4). No single physical explanation can explain all observations. We conclude that in some cases the H I may be distributed at large radii and therefore unable to cool to form H₂ which in turn would form new stars. Resolved H I imaging of a subset of this sample would therefore be interesting. Looking at the UV extent of this sample to seek low-level extended SF in what might be a low-density disc would also be interesting. In some cases, we may be seeing recent gas infall. The high fraction of kinematic misalignment and counter-rotation is the best evidence for this model. We can also interpret some of the kinematic misalignment as outflows/heating driven by AGN or stellar feedback, which may also be playing a role in suppressing SF in these H I-rich galaxies.

Galaxies are complex objects, and many physical processes are needed to explain their diversity of morphologies, masses, and SFRs (e.g. see Kormendy & Kennicutt 2004, for a review). This rare sample of H I-rich, but low-SF galaxies with resolved spectroscopy from the MaNGA survey presented an interesting puzzle alongside an opportunity to probe the processes quenching SF in some galaxies.

ACKNOWLEDGEMENTS

This publication acknowledges Haverford College Koshland Integrated Natural Sciences Center (KINSC)’s support in summer 2020 and summer 2021 research programmes through a Summer Research Grant.

This publication makes use of the SDSS data base. Funding for the SDSS-IV has been provided by the Alfred P. Sloan Foundation, the U.S. Department of Energy Office of Science, and the participating institutions. SDSS-IV acknowledges support and resources from the Center for High Performance Computing at the University of Utah. The SDSS website is www.sdss.org.

SDSS-IV is managed by the Astrophysical Research Consortium for the participating institutions of the SDSS Collaboration, including the Brazilian Participation Group, the Carnegie Institution

for Science, Carnegie Mellon University, Center for Astrophysics|Harvard & Smithsonian, the Chilean Participation Group, the French Participation Group, Instituto de Astrofísica de Canarias, the Johns Hopkins University, Kavli Institute for the Physics and Mathematics of the Universe (IPMU)/University of Tokyo, the Korean Participation Group, Lawrence Berkeley National Laboratory, Leibniz Institut für Astrophysik Potsdam (AIP), Max-Planck-Institut für Astronomie (MPIA, Heidelberg), Max-Planck-Institut für Astrophysik (MPA, Garching), Max-Planck-Institut für Extraterrestrische Physik (MPE), National Astronomical Observatories of China, New Mexico State University, New York University, University of Notre Dame, Observatório Nacional/MCTI, the Ohio State University, Pennsylvania State University, Shanghai Astronomical Observatory, United Kingdom Participation Group, Universidad Nacional Autónoma de México, University of Arizona, University of Colorado Boulder, University of Oxford, University of Portsmouth, University of Utah, University of Virginia, University of Washington, University of Wisconsin, Vanderbilt University, and Yale University.

This publication uses data products from the WISE, which is a joint project of the University of California, Los Angeles, and the Jet Propulsion Laboratory/California Institute of Technology, funded by the National Aeronautics and Space Administration.

The paper uses data from observations under project codes GBT16A_095, GBT17A_012, GBT19A_127, GBT20B_033, and GBT21B_130 using the GBT. The Green Bank Observatory is a facility of the National Science Foundation operated under cooperative agreement by Associated Universities, Inc.

This publication uses the MARVIN tool (Cherinka et al. 2019) to generate maps of galaxy properties from MaNGA.

This publication uses GZ2 data generated via the [Zooniverse.org](https://www.zooniverse.org) platform, development of which is funded by generous support, including a Global Impact Award from Google, and by a grant from the Alfred P. Sloan Foundation.

DATA AVAILABILITY

All MaNGA data (including all the value-added catalogues used in this work) are publicly available via the SDSS website. Other public datasets are used, with links given in text.

REFERENCES

- Abdurro’uf et al., 2022, *ApJS*, 259, 35
 Alatalo K. et al., 2014, *ApJ*, 795, 159
 Appleton P. N. et al., 2014, *ApJ*, 797, 117
 Martig M, Bournaud F, Teyssier R, Dekel A, 2009, *ApJ*, 707, 250
 Argudo-Fernández M. et al., 2015, *A&A*, 578, A110
 Baldwin J. A., Phillips M. M., Terlevich R., 1981, *PASP*, 93, 5
 Becker R. H., White R. L., Helfand D. J., 1995, *ApJ*, 450, 559
 Belfiore F. et al., 2016, *MNRAS*, 461, 3111
 Blanton M. R., Kazin E., Muna D., Weaver B. A., Price-Whelan A., 2011, *AJ*, 142, 31
 Blanton M. R. et al., 2017, *AJ*, 154, 28
 Brown M. J. I. et al., 2017, *ApJ*, 847, 136
 Bryant J. J. et al., 2019, *MNRAS*, 483, 458
 Bundy K. et al., 2015, *ApJ*, 798, 7
 Butsky I. S., Fielding D. B., Hayward C. C., Hummels C. B., Quinn T. R., Werk J. K., 2020, *ApJ*, 903, 77
 Cherinka B. et al., 2019, *AJ*, 158, 74
 Cheung E. et al., 2016, *Nature*, 533, 504
 Cluver M. E. et al., 2014, *ApJ*, 782, 90
 Cortese L. et al., 2012, *A&A*, 544, A101
 Cortese L., Catinella B., Cook R. H. W., Janowiecki S., 2020, *MNRAS*, 494, L42

- Davis T. A. et al., 2015, *MNRAS*, 449, 3503
 Doyle M. T., Drinkwater M. J., 2006, *MNRAS*, 372, 977
 Drory N. et al., 2015, *AJ*, 149, 77
 Duckworth C., Starkenburg T. K., Genel S., Davis T. A., Habouzit M., Kraljic K., Tojeiro R., 2020, *MNRAS*, 495, 4542
 Etherington J., Thomas D., 2015, *MNRAS*, 451, 660
 Fabian A. C., 2012, *ARA&A*, 50, 455
 Frank E., Stark D. V., Masters K., Roy N., Riffel R., Lacerna I., Riffel R., Bizyaev D., 2023, *MNRAS*, 519, 3312
 Grossi M. et al., 2009, *A&A*, 498, 407
 Gunn J. E. et al., 2006, *AJ*, 131, 2332
 Hallenbeck G. et al., 2014, *AJ*, 148, 69
 Hallenbeck G. et al., 2016, *AJ*, 152, 225
 Hart R. E. et al., 2016, *MNRAS*, 461, 3663
 Haynes M. P. et al., 2018, *ApJ*, 861, 49
 Heckman T. M., Best P. N., 2014, *ARA&A*, 52, 589
 Huang S., Haynes M. P., Giovanelli R., Brinchmann J., 2012, *ApJ*, 756, 113
 Jin Y. et al., 2016, *MNRAS*, 463, 913
 Kennicutt R. C., Jr, 1998, *ApJ*, 498, 541
 Kewley L. J., Dopita M. A., 2002, *ApJS*, 142, 35
 Kewley L. J., Ellison S. L., 2008, *ApJ*, 681, 1183
 Kewley L. J., Groves B., Kauffmann G., Heckman T., 2006, *MNRAS*, 372, 961
 Kormendy J., Kennicutt R. C., Jr, 2004, *ARA&A*, 42, 603
 Law D. R. et al., 2015, *AJ*, 150, 19
 Law D. R. et al., 2016, *AJ*, 152, 83
 Law D. R. et al., 2021, *AJ*, 161, 52
 Lemonias J. J., Schiminovich D., Catinella B., Heckman T. M., Moran S. M., 2014, *ApJ*, 790, 27
 Liao S., Gao L., 2019, *MNRAS*, 485, 464
 Masters K. L. et al., 2011, *MNRAS*, 411, 2026
 Masters K. L. et al., 2012, *MNRAS*, 424, 2180
 Masters K. L. et al., 2019, *MNRAS*, 488, 3396
 Meidt S. E. et al., 2013, *ApJ*, 779, 45
 O'Donnell J. E., 1994, *ApJ*, 422, 158
 Osterbrock D. E., Ferland G. J., 2006, *Astrophysics of Gaseous Nebulae and Active Galactic Nuclei*, 2nd edn. University Science Books, Mill Valley, CA. 978-1891389344.
 Parkash V., Brown M. J. I., Jarrett T. H., Fraser-McKelvie A., Cluver M. E., 2019, *MNRAS*, 485, 3169
 Peng Y.-j. et al., 2010, *ApJ*, 721, 193
 Rathore H., Kumar K., Mishra P. K., Wadadekar Y., Bait O., 2022, *MNRAS*, 513, 389
 Ristea A. et al., 2022, *MNRAS*, 517, 2677
 Roy N. et al., 2018, *ApJ*, 869, 117
 Saintonge A., Catinella B., 2022, *ARA&A*, 60, 319
 Saintonge A. et al., 2012, *ApJ*, 758, 73
 Saintonge A. et al., 2016, *MNRAS*, 462, 1749
 Sánchez S. F., 2020, *ARA&A*, 58, 99
 Sánchez S. F. et al., 2018, *Rev. Mex. Astron. Astrofis.*, 54, 217
 Schrubba A. et al., 2011, *AJ*, 142, 37
 Sellwood J. A., Masters K. L., 2022, *ARA&A*, 60, 36
 Shapiro G., Stark D. V., Masters K. L., 2022, *Res. Notes Am. Astron. Soc.*, 6, 1
 Smee S. A. et al., 2013, *AJ*, 146, 32
 Stark D. V. et al., 2021, *MNRAS*, 503, 1345
 Starkenburg T. K., Sales L. V., Genel S., Manzano-King C., Canalizo G., Hernquist L., 2019, *ApJ*, 878, 143
 Thilker D. A. et al., 2010, *ApJ*, 714, L171
 Verley S. et al., 2007, *A&A*, 472, 121
 Wake D. A. et al., 2017, *AJ*, 154, 86
 Wang H. et al., 2016, *ApJ*, 831, 164
 Westfall K. B. et al., 2019, *AJ*, 158, 231
 White S. D. M., Rees M. J., 1978, *MNRAS*, 183, 341
 Willett K. W. et al., 2013, *MNRAS*, 435, 2835
 Wright E. L. et al., 2010, *AJ*, 140, 1868
 Xu H. et al., 2022a, *MNRAS*, 511, 4685
 Xu Y., Luo Y., Kang X., Li Z., Li Z., Wang P., Libeskind N., 2022b, *ApJ*, 928, 100
 Yan R., Blanton M. R., 2012, *ApJ*, 747, 61
 Yan R. et al., 2016a, *AJ*, 151, 8
 Yan R. et al., 2016b, *AJ*, 152, 197
 Zhang K. et al., 2017, *MNRAS*, 466, 3217
 Zhang C. et al., 2019, *ApJ*, 884, L52
 Zhou Y., Chen Y., Shi Y., Gu Q., Wang J., Bizyaev D., 2023, *MNRAS* submitted ([arXiv:2303.00384](https://arxiv.org/abs/2303.00384))
 Zinger E. et al., 2020, *MNRAS*, 499, 768

This paper has been typeset from a $\text{\TeX}/\text{\LaTeX}$ file prepared by the author.